Characterization of a 5 mm thick CZT-Timepix3 pixel detector for energy-dispersive *γ*-ray and particle tracking

Physica Scripta

PAPER

Characterization of a 5 mm thick CZT-Timepix3 pixel detector for energy-dispersive γ-ray and particle tracking

P Smolyanskiy[1,*], B Bergmann[1], P Burian[1,2], A Cherlin[3], J Jelínek[1,4], D Maneuski[5], S Pospíšil[1] and V O'Shea[5]

[1] Institute of Experimental and Applied Physics, Czech Technical University in Prague, Husova 240/5, 11000 Prague, Czech Republic
[2] Faculty of Electrical Engineering, University of West Bohemia, Univerzitni 26, 30100 Pilsen, Czech Republic
[3] Kromek Ltd, County Durham, Sedgefield, TS21 3FD, United Kingdom
[4] Department of Nuclear and Particle Physics, University of Geneva, CH-1211, Geneva, Switzerland
[5] SUPA School of Physics and Astronomy, University of Glasgow, Glasgow, G12 8QQ, United Kingdom
[*] Author to whom any correspondence should be addressed.

E-mail: petr.smolyanskiy@cvut.cz

Keywords: CZT, Timepix3, gamma spectroscopy, particle tracking

OPEN ACCESS

RECEIVED
23 May 2023

REVISED
1 November 2023

ACCEPTED FOR PUBLICATION
29 November 2023

PUBLISHED
11 December 2023

Abstract

The present manuscript describes a comprehensive characterization of a novel highly segmented 5 mm CZT sensor attached to Timepix3. First, the sensor's IV curve was measured and basic sensor characterization was done with laboratory γ-radiation sources. The sensor resistivity was determined to be (0.155± 0.02) GOhm · cm. The sensor showed decent homogeneity, both for the per-pixel count rate and electron mobility-lifetime product $\mu_e\tau_e$. The latter was measured to be $\overline{\mu_e\tau_e} = 1.3 \times 10^{-3}$ cm^2/V with a standard deviation $\sigma = 0.4 \times 10^{-3}$ cm^2/V describing the dispersion of values for different pixels. The basic sensor characterization is complemented by measurements at grazing angle in a 120 GeV/c at the CERN's Super Proton Synchrotron. The penetrating nature of these particles together with the pixelation of the sensor allows for a determination of the charge collection efficiency (CCE), as well as charge carrier drift properties (drift times, lateral charge cloud expansion) as a function of the interaction depths in the sensor. While CCE drops by 30%–40% towards the cathode side of the sensor, from the drift time dependency on interaction depth, the electron mobility μ_e was extracted to be (944.8 ± 1.3) cm^2/V/s and $\tau_e = (1.38 \pm 0.31)$ μs. The spectroscopic performance was assessed in photon fields and extracted from energy loss spectra measured at different angles in the pion beam. While at photon energies below 120 keV incomplete charge collection leads to an underestimation of the photon energy when irradiated from the front-side, at higher energies the relative energy resolution was found to be ~4.5%, while a relative energy resolution of ~7.5% was found for the particle energy loss spectra. It is shown that the drift time information can be used to reconstruct particle interactions in the sensor in 3D, providing a spatial resolution of $\sigma_{xyz} = 241$ μm within the sensor volume and a particle trajectory measurement precision $\Delta_{xyz} = 100$ μm, at a distance of 1 m from the sensor. We demonstrate by measurement with a ^{22}Na source, that the energy resolution combined with the 3D reconstruction allows for detection of γ-ray source location and polarity using Compton scattering within the sensor (Compton camera and scatter polarimeter).

1. Introduction

Medical and astroparticle physics applications require the detection of γ-rays or hard x-rays with high efficiency, high spatial and temporal resolution. For example in medical imaging modalities, an improvement of the detection efficiency of the highly segmented sensor is often directly proportional to the reduction of the dose administered to the patient. Similarly, astroparticle physics experiments will profit from a reduction of observation times, while an increased sensitivity could lead to the detection of yet unobserved γ-sources. Hybrid

pixel detectors are interesting tools for use in these research areas owing to their single photon counting capability and a relatively small pixel pitch. One of the widespread readout chips for hybrid pixel detectors is the Timepix3 ASIC (Application-Specific Integrated Circuit) [1], developed within the Medipix3 collaboration [2]. A per-pixel (simultaneous) determination of the energy deposition and arrival time of a particle, makes Timepix3 detectors useful tools for many applications in fundamental research and life-sciences [3].

Depending on the application, the Timepix3 ASIC can be combined with silicon (Si), gallium arsenide doped with chromium (GaAs:Cr), and cadmium telluride (CdTe) or cadmium zinc telluride (CZT) sensors. Each material has both advantages and disadvantages. For example, for X- or γ-ray detection, the main disadvantage of the Si sensor material is the limited energy range to absorb a photon fully. Thus, high-Z material has been evaluated for spectral x-ray imaging and spectral micro-CT [4]. With recent analysis methodology improvement towards a 3D reconstruction of particle interactions within the semiconductor sensors [5, 6], enabled by the nanosecond-scale time resolution combined with a highly-segmented sensor, CdTe sensors were evaluated for use as single-layer Compton Cameras to search for locations of γ-radiation sources [7–9].

Pixel detectors based on CdTe or CZT typically feature thicknesses up to 2 mm and profit from a larger absorption efficiency in the photon energy range above ~100 keV [10]. Currently, the thickest sensor evaluated with Timepix [11] family ASIC is a 3 mm thick CdTe sensor [12]. Higher photon sensitivity is desirable for example for environment monitoring, (low-flux) Compton camera applications or in positron emission tomography (PET) and can be achieved by further increasing the thickness of the sensor. However, in this case, the characteristics of the detector can degrade due to charge trapping, a nonlinearity of the electric field, and the charge sharing effect [13]. An additional disadvantage of these high-Z materials (GaAs:Cr, CdTe and CZT) is that x-ray fluorescence (XRF) photons can escape the pixels, which smears the x-ray image and decreases the energy resolution of the detector. Moreover, polarization effects lead to time-dependent disturbances of the electric fields and charge collection across the sensor in high-rate conditions [14, 15]. Moreover, 3D reconstruction in the dense solid-state sensor provides a decent trajectory reconstruction precision, impact angle determination and particle identification with compact devices [5], thus allowing for application with strict requirements on size, weight and power consumption.

This work presents a comprehensive investigation of a 5 mm thick CZT highly segmented (pixel pitch of 110 μm) sensor attached to Timepix3, aiming at providing novel insights into material properties, which allow for subsequent implementation into simulation. These will be used to optimize the detector design parameters (e.g. pixel pitch), adapt data analysis methodology, and propose multi-layer systems for specific applications. The basic sensor characterization measurements, discussed in sections 4.1, 4.2, 4.3, are complemented by measurements in penetrating particle beams studying charge transport properties (in sections 4.4, 4.5) and the impact of the charge sharing effect (in section 4.6). A discussion of the device's spectroscopic performance and particle trajectory reconstruction precision, in sections 4.7 and 5.1, respectively, leads to the conclusions (section 6).

2. Materials and methods

2.1. Timepix3 detector with CZT sensor

The detector investigated in this work (see figure 1(a)) consists of a Timepix3 ASIC hybridized with a 5 mm thick CZT sensor produced by Kromek Ltd [16]. The crystal was grown using the Traveling Heater Method. The sensor has Pt Schottky contacts.

The Timepix3 chip provides time binning of 1.56 ns, allows data-driven readout, and simultaneous measurement of the energy and time in each of its 256 $\times$ 256 square pixels with dimensions of 55 $\times$ 55 μm^2. A pixel pitch of 110 μm is featured by the sensor and chip in our case (only a quarter of the chip pixels are connected to the sensor). Ionizing radiation passing through the reverse biased sensor creates free charge carriers (electrons and holes), which then drift towards the electrode with the opposite charge. During the drift motion, a current signal is induced at the pixels closest to the carrier position, which is shaped, amplified and then compared to a set threshold (THL).

The time, when the pulse crosses THL on the upwards slope then defines ToA (Time-of-Arrival). At the same time, the Time-over-Threshold (ToT) measurement is initiated, which is then stopped by the signal crossing THL on its downward slope. ToT is sampled with a continuously running 40 MHz clock and can be related to energy after per-pixel calibration with well defined photon energies (usually fluorescence x-rays). The ToA sampling is done with a 640 MHz clock from a local oscillator, thus achieving a time granularity of 1.56 ns.

For detector control and read out, the Katherine interface [17] was used. The sensor bias voltage was supplied from a high voltage power supply Iseg SNR. The so-called low power mode of the chip was used to ensure the lower operating temperature of the detector. Moreover, in this mode the peaking time of preamplifier

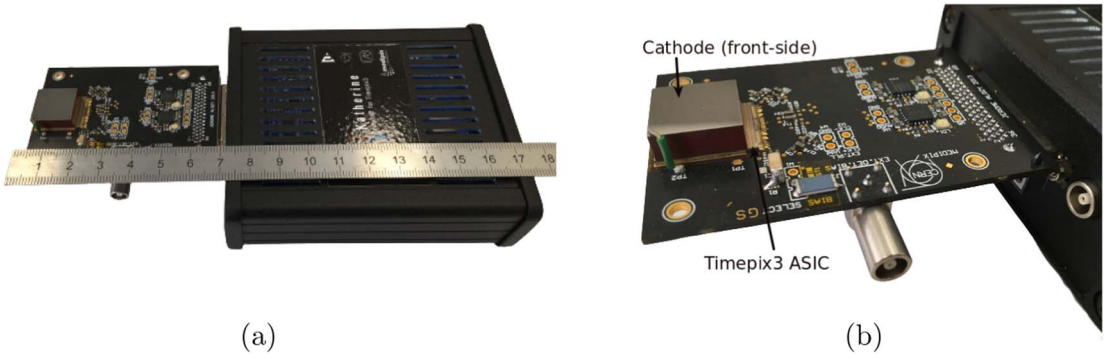

Figure 1. (a) Photograph of the Timepix3 ASIC with a 5 mm thick CZT sensor with the used readout electronics; (b) detailed view of the detector.

is higher than for standard settings, ∼150 ns, which means that the ballistic deficit is not significant even for measurements at low bias voltages.

The per-pixel ToT-energy calibration was done with fluorescence x-rays (Zr, Cd, Sn) and characteristic γ-rays (^{241}Am source) as described in [18]. In order to suppress the influence of charge losses, the sensor was irradiated from the pixel-side which is opposite to the front-side (see figure 1(b)). The threshold was set at 8 keV, which represented the lowest level at which the detector operated without introducing noise. The applied bias voltage was set at -1200 V during the calibration.

3. Experiment design and data analysis

3.1. Basic sensor characterization

3.1.1. IV characteristics

Before performing any tests with the radioactive sources the IV characteristic of the CZT sensor was measured with high voltage power supply Iseg SNR. The bias voltage U_{bias} was varied in the range of [–1500, 0] V at room temperature ($T = 21\ ^{o}$C) while the readout chip was switched off.

3.1.2. Mobility-lifetime product measurements

The mobility-lifetime $\mu_e\tau_e$ product of electrons was measured using the well-known technique based on the Hecht equation. It was modified to account for the small pixels [19]. The detector was illuminated by a ^{241}Am source from the front-side (cathode side). More than 90% of 60 keV photons are absorbed in less than 1 mm of CZT, so that the charge transport properties can be investigated almost for the full thickness of the sensor. In order to create the spatial map of $\mu_e\tau_e$ product over pixels, the energy spectra recorded by each pixel were analyzed at different bias voltages. The photopeaks were fitted by a gaussian and the obtained means $E_{\text{meas}}^{\text{Am}-\text{photo}}$ were plotted against the bias voltage U_{bias}. The dependencies of $E_{\text{meas}}^{\text{Am}-\text{photo}}$ versus U_{bias} for each pixel then were fitted by the modified Hecht function [19].

3.2. Charge transport studies in the 120 GeV/*c* pion beam

The detector was exposed to a 120 GeV/c pion beam at the Super-Proton-Synchrotron (SPS) at CERN. Beam particles were impinging on the sensor at 50 degrees with respect to the sensor normal. Such particles are close to the minimum ionizing particles providing a uniform energy deposition across the particle track length within the sensor. The sensor bias voltage was varied in the range from −600 V to −1800V. In addition, an angle scan was performed (0, 30, 60, 75 and 90 degrees to the sensor normal) at a bias voltage of −1000 V.

The raw detector response to 120 GeV/c pion beam at an impact angle of 50 degrees in the form of 2D projections of pion tracks is shown in figure 2. Pion tracks (clusters) are typically 2-4 pixels wide lines parallel to X-axis, sometimes accompanied by outgoing δ-rays. Background particles (γ-rays, electrons) having different morphology and energy deposition per cluster can be filtered out. In order to select only pion tracks for further analysis the cuts on the following cluster characteristics were applied:

- the sum of all pixel energies within a cluster (*cluster energy*) $E_{\text{cluster}} \in [4500, 7500]$ keV,
- the number of pixels forming a cluster (*cluster size*) $N_{\text{pixels}} \in [105, 160]$ pixels, and
- the distance between the exit and entry points of the tracks (*cluster length*) $L \in [52, 57]$ pixels.

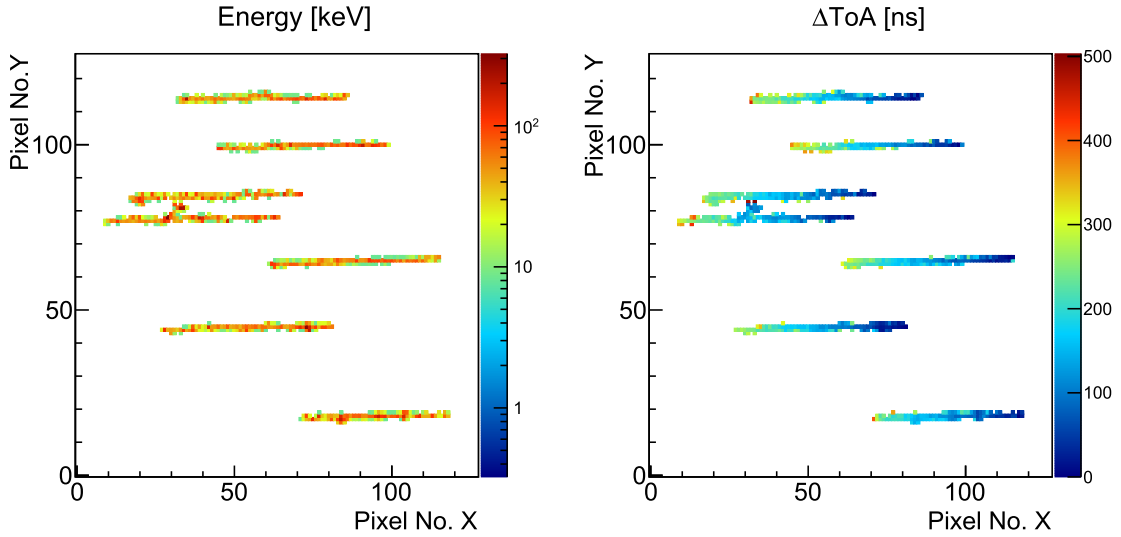

Figure 2. Per-pixel energy deposition (left) and the relative time differences within single clusters (right) for typical particle tracks measured in the pion beam at an impact angle of 50 degrees. The pions tracks were selected using the cuts mentioned in section 3.2.

To explore the charge transport properties of the CZT material, the dependencies of the electron drift time and the Charge Collection Efficiency (CCE) on the interaction depth were measured for different bias voltages. Therefore, the depth coordinate z was calculated by linear interpolation between the exit x_{exit} and entry points x_{entry} of a selected pion-like cluster:

$$z(x) = \frac{d}{L} \times r(x), \tag{1}$$

where $d = 0.5$ cm is the detector thickness, $L = |x_{\text{entry}} - x_{\text{exit}}|$ is the projected core track length, $r(x) = |x - x_{\text{exit}}|$ is the projected distance of point x along core track. To be consistent with previous publications, $z = 0$ is defined as the plane of the pixelated anode and $z = d$ is the front-side plane (common cathode). The sensor thickness was divided into 50 equal-depth bins. Further details on the track analysis used for depth reconstruction are described in detail in [6].

The Timepix3 chip provides the timestamp t in each pixel. Thus, if the pion track enters the sensor at an angle with respect to the sensor normal, by calculating the difference of the pixel x's timestamp t_x and the minimal time t_0 within a track, the drift time dependence on the interaction depth $z(t_{\text{drift}} = t_x - t_0)$ can be obtained. Here, the drift time is not the time needed for charge carriers to reach the pixel electrodes, but it is the time at which the induced signal from the charge carriers rises above the set in the chip threshold.

3.3. Charge sharing study in the 120 GeV/*c* pion beam

Charge sharing is a well-known effect in detectors constituted by small pixels [20]. In the case of thick sensors (in our case the sensor thickness is 5 mm) it is even stronger in comparison with conventional sensors (with thicknesses between 300 μm—2 mm), because of the lateral diffusion of the charge carriers during their longer drift towards the pixel electrodes. While the charge sharing effect can be used to achieve sub-pixel spatial resolution [21], it degrades the energy resolution of the detector, even if the full deposited energy of the particle track is restored through the clustering, since some amount of charge can be lost between the pixel electrodes or fall below the energy threshold of the detector at the cluster boundaries.

In order to investigate the impact of charge sharing in a 5 mm thick CZT-Timepix3 detector, we applied the approach adapted from [22]. The method is based on the determination of how the track from the minimum ionizing particle expands in a lateral direction passing through the sensor at a grazing angle. For analysis, the data set with 120 GeV/c pions at an impact angle of 60 degrees with respect to the sensor normal at a bias voltage of -1000 V was taken. The tracks were filtered using the following energy, size, and length attributes of the clusters: $E_{\text{cluster}} \in [6000, 10\,000]$ keV, $N_{\text{pixels}} \in [140, 210]$ pixels, and $L \in [77, 83]$ pixels.

3.4. Measurement with laboratory γ-sources

Measurements in the particle beam are complemented by laboratory studies with γ-radiation sources studying the achievable energy resolution. Measurements were performed with ^{241}Am, ^{152}Eu and ^{22}Na sources. The sources were placed at the distance of 10 cm from the detector to have a diffuse irradiation across the whole detector surface. To study the capabilities to reconstruct the source location, additionally, the ^{22}Na was placed at

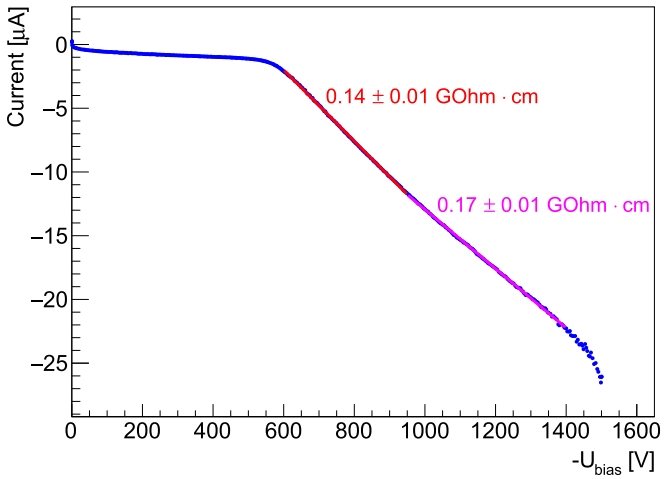

Figure 3. The IV characteristic of the sensor with two fitted linear parts.

a distance of approximately 10 cm at different lateral displacements (separated by 5 cm). While the bias scan with the ^{241}Am source shows an increase in energy resolution with increasing bias (figure 12(a)), the results are presented at a bias voltage of −1200 V, which provided a stable long-term measurement at an acceptable noise level. To understand the impact of incomplete charge collection, the detector was irradiated from the front-side and from the pixel-side.

4. Results

4.1. IV characteristic

The obtained IV curve (figure 3) has three main regions: from 0 to −550 V the leakage current is ∼1 μA, and from −550 to −1400 V the current increases by 2.5 μA for each 100 V. After −1400 V a fast increase of the leakage current can be observed. The resistivity was determined in two different parts of the IV curve ([–1400, –950] V and [–950, –600] V) as:

$$\rho = \frac{U_{\text{bias}}}{I} \times \frac{S}{d}, \tag{2}$$

where $S = 1.98$ cm^2 is the sensor area, $d = 0.5$ cm is the detector thickness. The average resistivity was found to be $\rho_{\text{mean}} = (0.155 \pm 0.02)$ GOhm · cm,

4.2. Mobility-lifetime product measurements

The measured mobility-lifetime $\mu_e\tau_e$ product of electrons is shown in figures 4(b) and (a) in the form of one- and two-dimensional histograms. The mean value of mobility-lifetime product across sensor is $\overline{\mu_e\tau_e}$ $= 1.3 \times 10^{-3}$ cm^2/V with a standard deviation $\sigma = 0.4 \times 10^{-3}$ cm^2/V. The value is of the same order of magnitude as that for other available CZT sensors [15].

4.3. Count rate homogeneity

To estimate the homogeneity of the sensor material, the number of detected events per pixel was determined using the dataset from measurements with ^{241}Am source. The results are shown at figures 5(a) and (b). Noisy pixels have a number of counts that is far from average. The right side of the illumination map is more blurred due to random noise from the chip (from time to time full chip columns with numbers from 70 to 110 appear to be noisy).

4.4. Drift time versus interaction depth

Figure 6 shows the drift time dependencies on the interaction depth for seven applied bias voltages. In all cases, the dependencies are almost linear which indicates the uniformity of the electric field across the sensor. Further, the linear parts of the measured dependencies were fitted to determine the drift velocities of the electrons V_{drift}. It is shown as a function of the electric field in figure 7. One can see that this dependence is linear with the electron mobility given by the slope: $\mu_e = (944.8 \pm 1.3)$ cm^2/V/s. Combining this value with the mobility-lifetime value obtained in section 4.2, one can estimate the lifetime of electrons to be $\tau_e = (1.38 \pm 0.31)$ μs, which is similar to the values reported by [15].

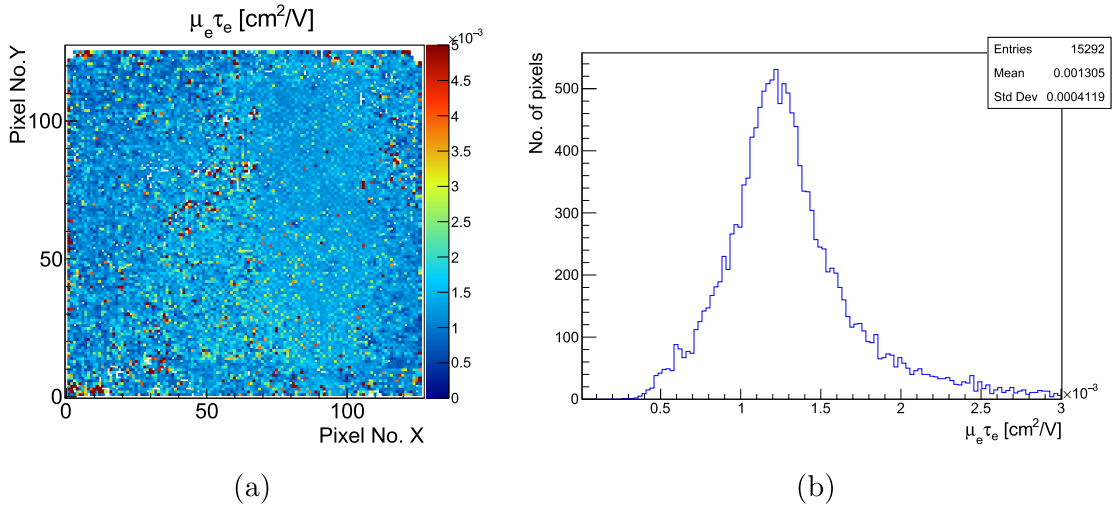

Figure 4. (a) Mobility-lifetime $\mu_e\tau_e$ product mapped across the pixel matrix; (b) Distribution of the mobility $\mu_e\tau_e$ product for all pixels.

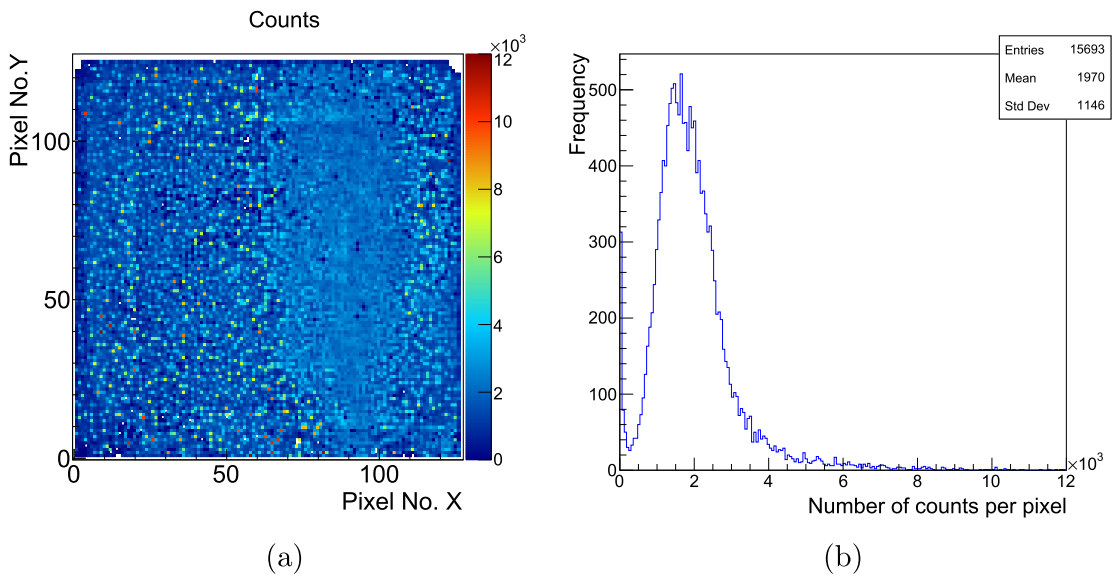

Figure 5. (a) The count rate homogeneity map of the sensor as measured with a ^{241}Am source; (b) Distribution of measured per-pixel count rate.

4.5. Charge collection efficiency versus interaction depth

The same methodology described in the previous section was applied to the data to extract the CCE dependence on the interaction depth. But, instead of time, the energy information from the pixels was utilized. For each depth bin the measured energy deposition was divided by the nominal energy deposition $E_{\text{nominal}} = 70$ keV. Figure 8 shows the dependence of the CCE on the interaction depth for different bias voltages. Overall, a degradation of the CCE through the depth towards the common electrode can be observed. The CCE drop of 30%–40% is caused by the trapping of charge carriers on different defects of the CZT crystal.

4.6. Charge cloud size versus interaction depth

Figure 9 shows an example of 120 GeV/c pion track (impinging the sensor at 60 degrees to the sensor normal) fitted with a linear function to determine the track's azimuth angle and the position along the particle trajectory with subpixel resolution. For tracks taken for analysis, lateral pixels triggered by δ-electrons were removed, while high energy values in some pixels (caused by noise behavior or Landau fluctuations) have been replaced by the median value over the track. Thus, better fitting quality was achieved. Only tracks tilted at $\pm$ (1–3) degrees with respect to the x-axis were selected for further analysis providing the best fitting precision.

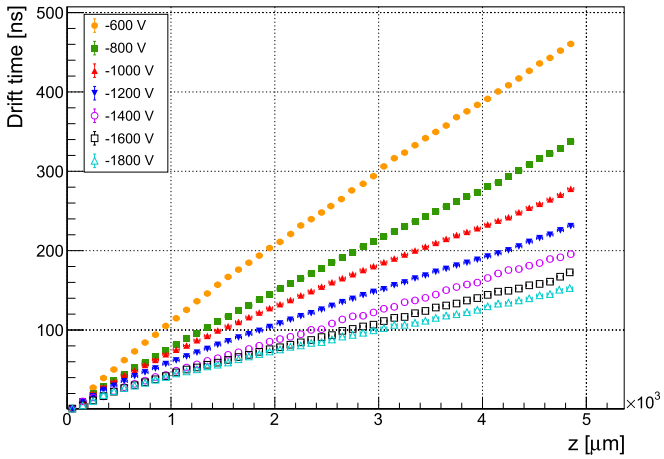

Figure 6. The dependence of the electron drift time on the interaction depth for different bias voltages. Coordinate $z = 0$ μm corresponds to the pixelated side of the detector.

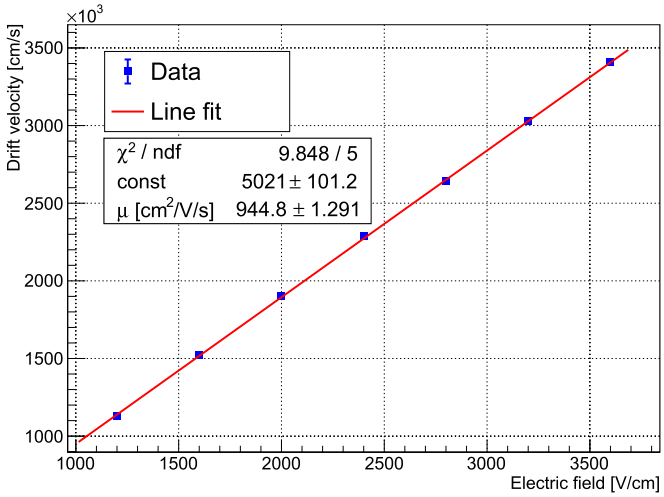

Figure 7. The electron drift velocity as a function of the electric field.

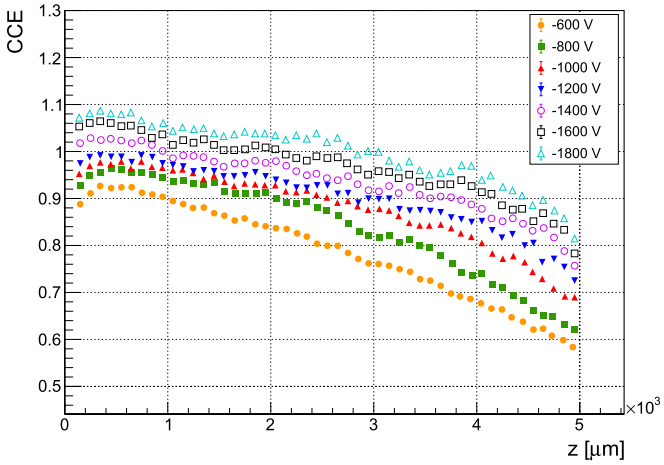

Figure 8. The dependence of the charge collection efficiency on the interaction depth for different bias voltages. Coordinate $z = 0$ μm corresponds to the pixelated side of the detector.

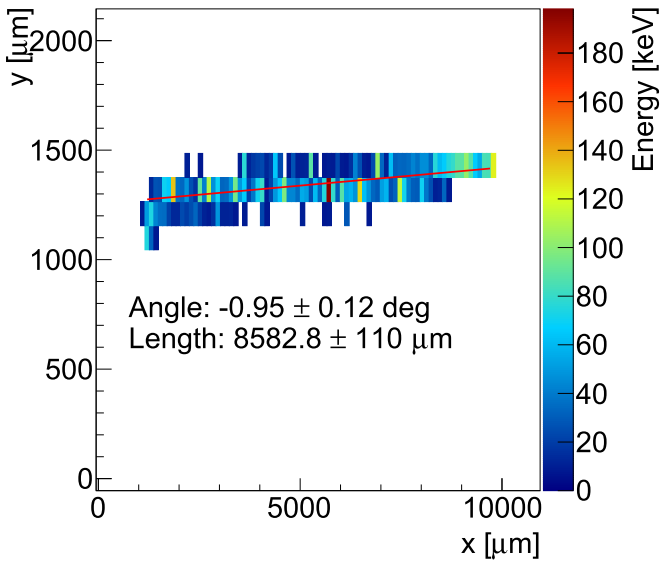

Figure 9. Example of a 120 GeV/c pion track fitted with a linear function.

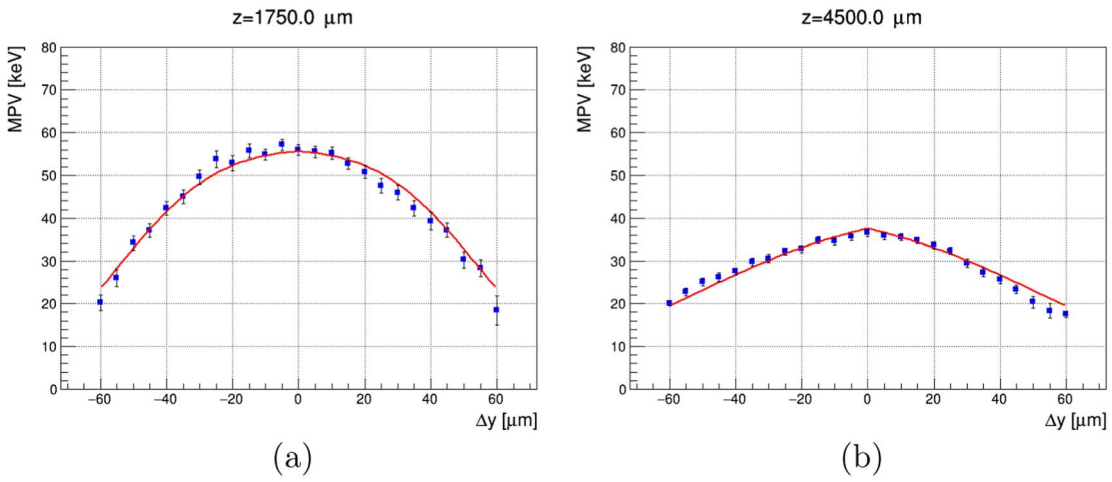

Figure 10. The lateral charge deposition profile measured at depth $z = 1.75$ mm (a) and $z = 4.5$ mm (b).

Instead of depth coordinate determination from the geometry (how it was done in [22]) it was determined from the look-up table measured as described in section 4.4 for the bias voltage of −1000 V. For each depth bin, the energy deposition was determined by fitting the corresponding spectrum by a convolution of a Landau curve and a Gaussian. Then, for each x coordinate (which can be used to calculate a corresponding z coordinate) of the track the deviation Δy_z between detected y position and the position y_{subpixel} determined by fitting: $\Delta y_z = y - y_{\text{subpixel}}$. Combining the measured energy information (or induced charge) C_z in each bin z with position Δy_z it is possible to create the lateral charge deposition profile of pixel for different depths. Such dependencies can be fitted by the function [22]:

$$C_z \sim \frac{C_{0,z}}{2} \times \left[1 + \text{Erf}\left(\frac{p/2 - \Delta y_z}{\sqrt{2}\,\sigma(z)}\right)\right], \tag{3}$$

where $C_{0,z}$ is the most probable value of Landau fluctuations of the energy deposition, $p = 110$ μm is the pixel pitch, $\sigma(z)$ describes the Gaussian spread of the transverse profile of the charge carrier cloud. Figures 10(a) and (b) show the lateral charge deposition profiles for depth bins 1.75 mm and 4.5 mm, which are fitted by equation (3). The extracted values of $\sigma(z)$ are: $\sigma(z = 1.75\text{ mm}) = (25.8 \pm 1.7)$ μm and σ $(z = 4.5\text{ mm}) = (43.1 \pm 2.8)$ μm. For the region close to pixels the width of the transverse profile of the charge carrier cloud is larger than for the region close to the common electrode. This shows the higher contribution of the charge sharing. Also, one can note that the amplitude of these dependencies is different, which is connected

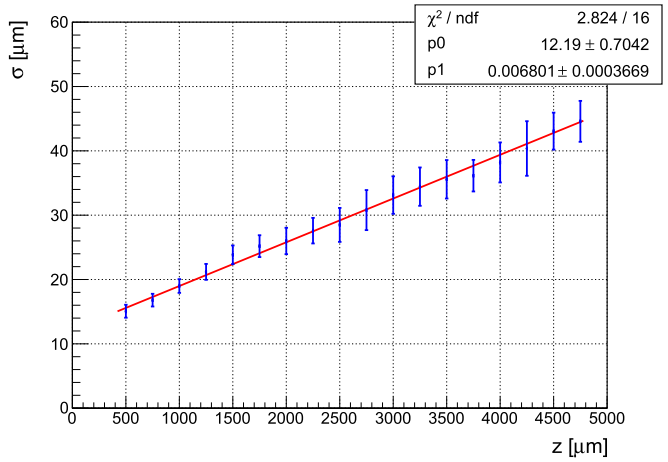

Figure 11. The dependence of the charge cloud profile width $\sigma(z)$ on the interaction depth z for bias voltage of −1000 V.

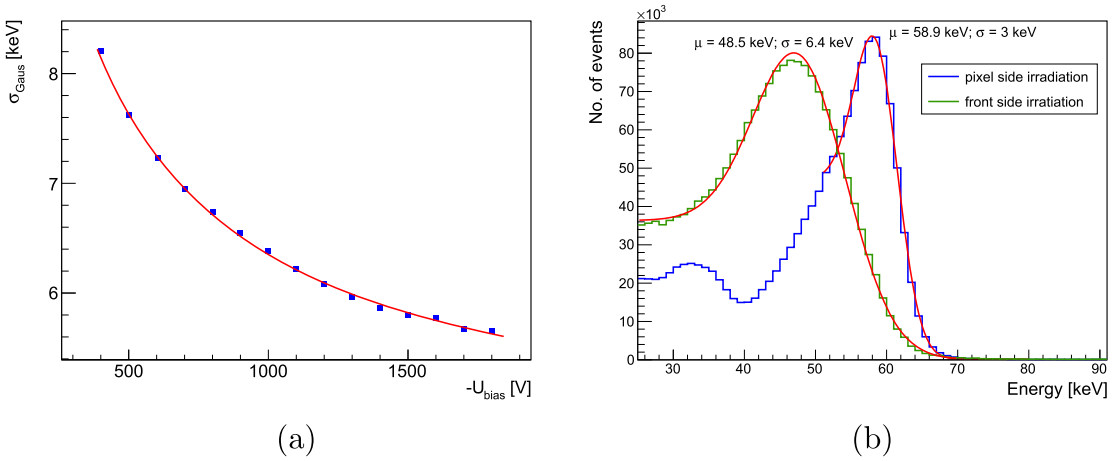

Figure 12. (a) Energy resolution σ_{Gauss} as a function of the bias voltage measured with a ^{241}Am source (front-side irradiation); (b) Measured energy spectrum of a ^{241}Am source for irradiation from the pixel-side and from the front-side at a bias of −1200 V. The photo-peak was modeled with a Gaussian on top of an error-function.

with the charge losses during the drift of charge carriers from the interaction point towards pixels as already shown in section 4.5.

The resulting dependency of the charge cloud profile width $\sigma(z)$ on the interaction depth z is shown in figure 11. It shows that if the interaction occurs close to the common electrode the induced charge is most likely to be shared between the neighboring pixels. The determined $\sigma(z)$ dependence includes all contributions to the spatial expansion of the charge cloud: lateral diffusion, repulsion of the charge carriers, and (possibly) capacitive coupling between pixels. The presented experimental dependence can be used for fast detector response simulation, where the initial position of the charge cloud is projected to the pixel matrix with corresponding $\sigma(z)$. It is important to note that the result relies on several major factors: the deposited energy since the initial charge cloud size is dependent on the energy and the bias voltage because it affects the lateral diffusion.

4.7. γ- and particle energy loss spectroscopy

To determine the achievable energy resolution in γ-spectroscopy, measurements were performed with ^{241}Am, ^{152}Eu and ^{22}Na sources. While the bias scan with the ^{241}Am source shows an increase in energy resolution with increasing bias (figure 12(a)), the results are presented at a bias voltage of −1200 V, which provided stable long-term measurement at an acceptable noise level. To understand the impact of incomplete charge collection, the detector was irradiated from the front-side and from the pixel-side. Figure 12(b), figure 13, and figure 14 show the resulting spectra for ^{241}Am, ^{152}Eu and ^{22}Na, respectively. The spectral peak positions were determined by fitting a Gaussian distributions on top of an error-function for ^{241}Am ($f_{\text{Erf}}(E)$), while a linear background model was chosen for the photo-peaks ($f_{\text{Linear}}(E)$) and Compton-edges in the ^{152}Eu and ^{22}Na spectra ($f_{\text{Compton}}(E)$):

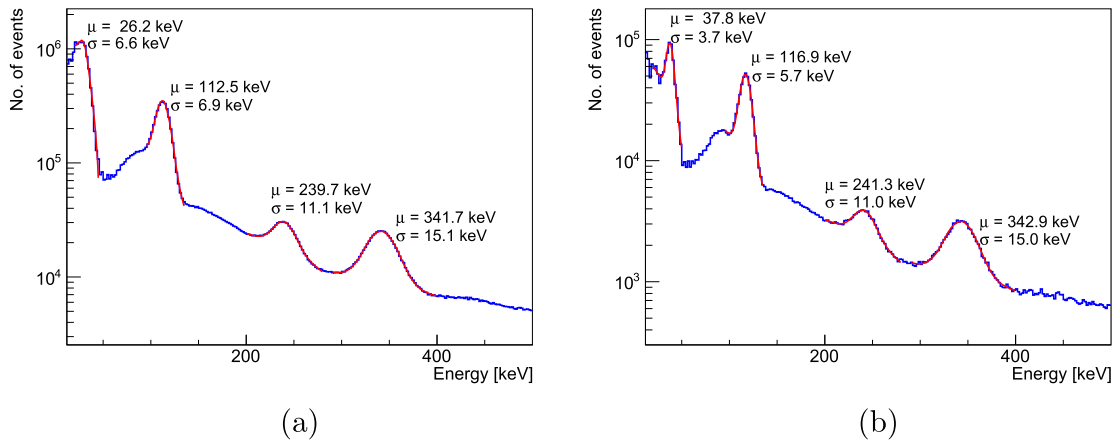

Figure 13. Measured energy spectrum of ^{152}Eu irradiated from the front-side (a) and from the pixel-side (b). Fitting Gaussian curves with a linear background model was used to determine the peak positions and the energy resolution. Due to incomplete charge collection, up ~116 keV, peak shifts are observed for front-side irradiation. The bias was set at -1200 V.

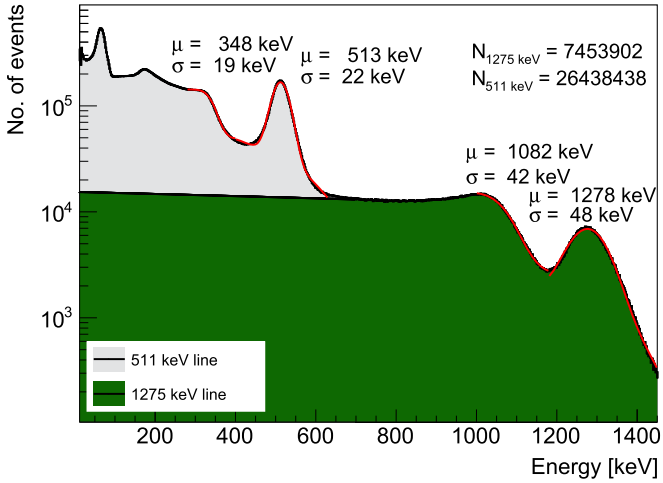

Figure 14. ^{22}Na energy spectrum (front-side irradiation only is shown, since peaks of interest have high enough energy to not demonstrate front-side/pixel-side asymmetry). A linear extrapolation of the 1275 keV line's Compton continuum towards lower energy was used to determine the number of clusters related to the 1275keV line (indicated by the green area) and the 511 keV annihilation signal (gray area). Positions of the Compton edges and photo peaks were determined with error-function and Gaussian fits, both on a linear background. The bias was set at -1200 V.

$$f_{\mathrm{Erf}}(E) = a \times \exp\left(-\frac{(E-\mu)^2}{\sigma^2}\right) + \frac{b}{2}\left[1 - \mathrm{Erf}\left(\frac{E-\mu}{\sqrt{2}\,\sigma}\right)\right], \tag{4}$$

$$f_{\mathrm{Linear}}(E) = a \times \exp\left(-\frac{(E-\mu)^2}{\sigma^2}\right) + b \times E + c, \tag{5}$$

$$f_{\mathrm{Compton}}(E) = \frac{a}{2}\left[1 - \mathrm{Erf}\left(\frac{E-\mu}{\sqrt{2}\,\sigma}\right)\right] + b \times E + c, \tag{6}$$

where a, b, c are fit parameters.

The fit results are summarized in table 1. For photons with energies ~120 keV one can see an underestimation of the measured peak positions and a worse energy resolution when the detector is irradiated from the front-side. It is caused by an incomplete charge collection from the shallow interaction depths (see section 4.5). At higher photon energies, this front-side/pixel-side asymmetry is no longer observable and the relative energy resolution stabilizes at ~4.5%. These results can be compared with a previously published study [12] finding the energy resolution (σ_{Gauss}) for a 3 mm thick CdTe sensor with similar granularity (55 μm pixel pitch) to be 6.7 keV (11.3%) at 59.5 keV, 7.1 keV (5.8%) at 122 keV, 54.1 keV (8.2%) at 662 keV. While a similar resolution is found at the lower investigated energy range, a significantly better spectroscopic performance was achieved with an investigated device at higher energies.

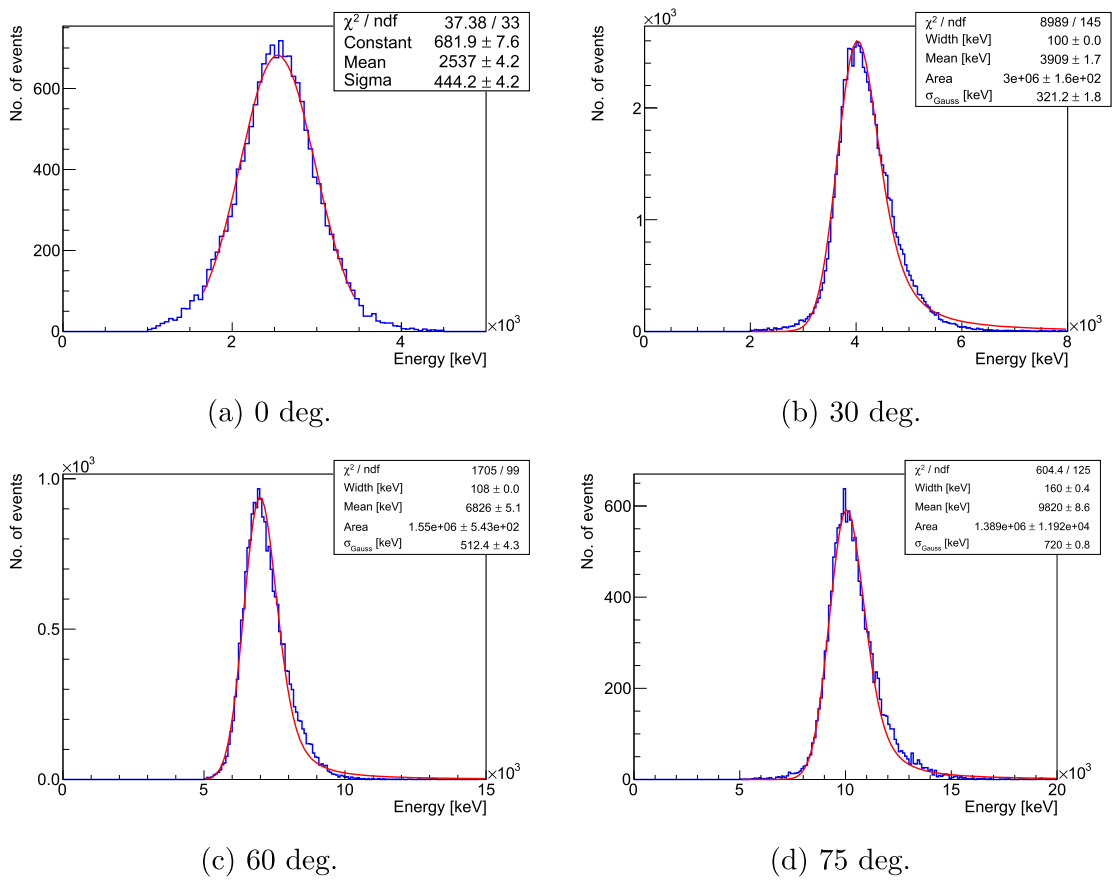

Figure 15. Energy deposition spectra measured after 120 GeV/c pion impact at different angles. The distributions were fitted with a Landau curve smeared by a Gaussian profile. The Gaussian width was interpreted as a conservative estimate of the achievable energy resolution.

Table 1. Peak positions E_{MPV} and energy resolution σ_{Gauss} extracted from measured γ- and energy-loss spectra.

Source	E_{MPV} [keV]	σ_{Gauss} [keV]	$\frac{\Delta E}{E} = \frac{\sigma_{\mathrm{Gauss}}}{E_{\mathrm{MPV}}}$ [%]
^{152}Eu (front/pixel-side irradiation)	26.2/36.8	6.6/3.7	25.2/10.1
^{241}Am (front/pixel-side irradiation)	48.5/58.9	6.4/3.0	13.2/5.0
^{152}Eu (front/pixel-side irradiation)	112.5/116.9	6.9/5.7	6.1/5.2
^{152}Eu (front-side irradiation)	240	11	4.6
^{152}Eu (front-side irradiation)	342	15	4.4
^{22}Na (front-side irradiation, compton edge)	348	19	5.6
^{22}Na (front-side irradiation)	513	22	4.3
^{22}Na (front-side irradiation, compton edge)	1082	42	3.9
^{22}Na (front-side irradiation)	1278	48	3.8
120 GeV/c pions—30 degrees (front-side irradiation)	3,909	321	8.2
120 GeV/c pions—60 degrees (front-side irradiation)	6,826	512	7.5
120 GeV/c pions—75 degrees (front-side irradiation)	9,820	720	7.3

The energy deposition spectra of 120 GeV/c pion tracks are shown in figure 15 for impact angles of 0, 30, 60 and 75 degrees. The spectra for impact angles of 30, 60 and 75 degrees are described by a Landau distribution convoluted with a Gaussian, whereby the latter is interpreted as the energy resolution of the detector. Table 1 summarizes the most probable energy losses E_{MPV} and the Gaussian fluctuations σ_{Gauss} extracted from the fits. Since the 5 mm thick sensor cannot be regarded as a thin sensor, Gaussian smearing can already be expected from the physics of the interaction. The presented resolution can thus be regarded as a conservative estimation. The relative energy resolution was defined as $\Delta E/E = \sigma_{\mathrm{Gauss}}/E_{\mathrm{MPV}}$ and found to be better than 9 % for all investigated angles. For the perpendicular impact of pions, the energy spectrum is distorted because the energy

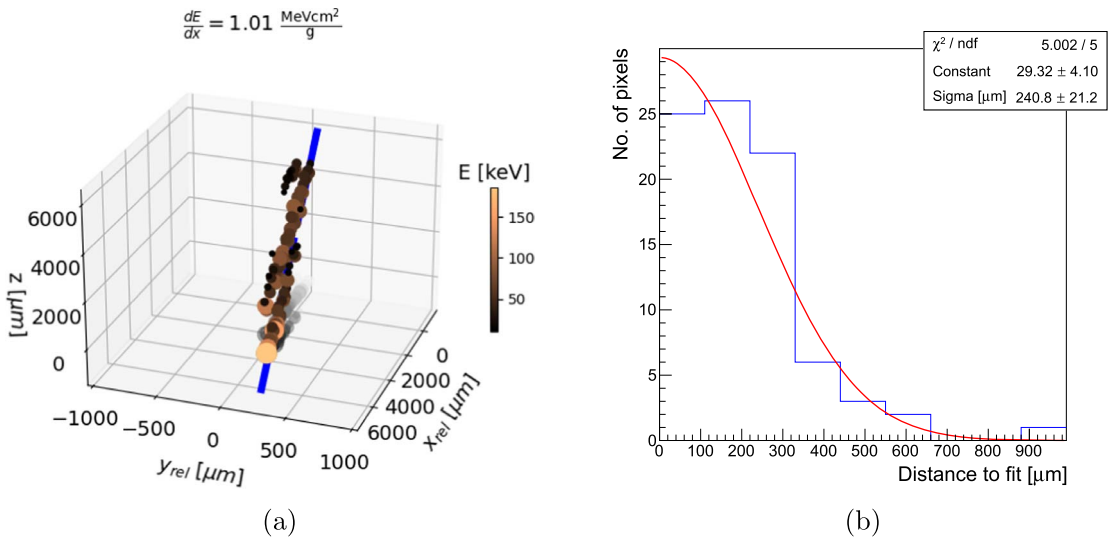

Figure 16. (a) 3D reconstruction of a 120 GeV/c pion passing through the sensor. The particle trajectory was determined by a 3D line fit. The color and size of the points indicate the energy deposition, while the z coordinate is further indicated by the grayscale projection of the points to the xy-plane. For visualization, the software from [24] was used. (b) Distribution of the distances of reconstructed points to the fitted trajectory with a Gaussian fit to determine the resolution σ_{xyz}.

deposition per pixel is higher than 500 keV, which is above the linear range of the Timepix3 preamplifier's response in electron collection mode [23].

5. Discussion

5.1. 3D reconstruction of particle trajectories

The pixelization together with measured look-up tables $z(t_{drift})$ (see section 4.4) allows 3D trajectory reconstruction of charged particle traces by adding the evaluated z coordinates to (x,y) coordinates of the chip. Figure 16(a) shows a 3D reconstructed 120 GeV/c pion trajectory obtained with the methodology outlined in [5, 6]. The reconstructed track was fitted with an iterative 3D Hough transform algorithm [24]. Fitting the distribution of the distances of measured points to the line fit (see figure 16(b)), the spatial resolution within the sensor volume was estimated to be $\sigma_{xyz} = 241\,\mu$m. Fitting the 3D line parametrization

$$\vec{r}(\lambda) = \vec{r}_0 + \lambda \times \vec{dr} = \begin{pmatrix} x_0 \\ y_0 \\ 0 \end{pmatrix} + \lambda \times \begin{pmatrix} dx \\ dy \\ 1 \end{pmatrix} \tag{7}$$

with the pivot point $\vec{r}_0$, the normalized directional vector $\vec{dr}$ and λ being a scalar describing the position along the line. Evaluating the errors of the fit parameters x_0, y_0, dx and dy, the trajectory reconstruction precision at a distance of 1 m to the sensor was found to be 100 μm. Even though with thinner sensors designs (500 μm and 2 mm) investigated in [5, 6] better resolutions σ_{xyz} were found, the increased thickness to pitch ratio provides a better pointing precision, in particular for impact close to the sensor normal.

5.2. Improved detection efficiency (for PET application)

The detection efficiency is determined from the ^{22}Na measurement as

$$\varepsilon_i = \frac{N_i}{\varepsilon_{geo} \times t_{exposure} \times P_{emission,\,i} \times A_0 \times \exp[-\lambda(t_{meas} - t_0)]}, \tag{8}$$

where $\varepsilon_{geo} = \frac{S}{4\pi h^2}$ denotes the geometric factor with the distance detector-source $h = (10.5 \pm 0.3)$ cm, S is the sensor area; $t_{exposure} = 6000$ s is the measurement time, $A_0 = 37.0$ MBq is the certified activity measured by the source manufacturer on November 1, 2019 (t_0), t_{meas} is the time when the experiment was carried out, and $\lambda = \frac{\ln(2)}{t_{1/2}}$ is the decay constant with $t_{1/2} = 2.6029(8)$ yrs [25]. $P_{emission}$ denotes the probability of the γ-ray emission per decay: $P_{emission,511\ keV} = 0.903(9)$ and $P_{emission,\ 1275\ keV} = 0.9994(13)$ [25]. The numbers of detected i-line (511 or 1275 keV) photons N_i were determined after spectrum decomposition by linearly extrapolating the 1275 keV line's Compton continuum towards lower energies and bin-wise count rate subtraction (see figure 14). To determine the photopeak efficiencies $\varepsilon_{photo,i}$, $N_{photo,i}$ is calculated from the Gaussian fit parameters of equation (6) as $N_{photo,i} = \sqrt{2\pi}\, a_i \sigma_i$.

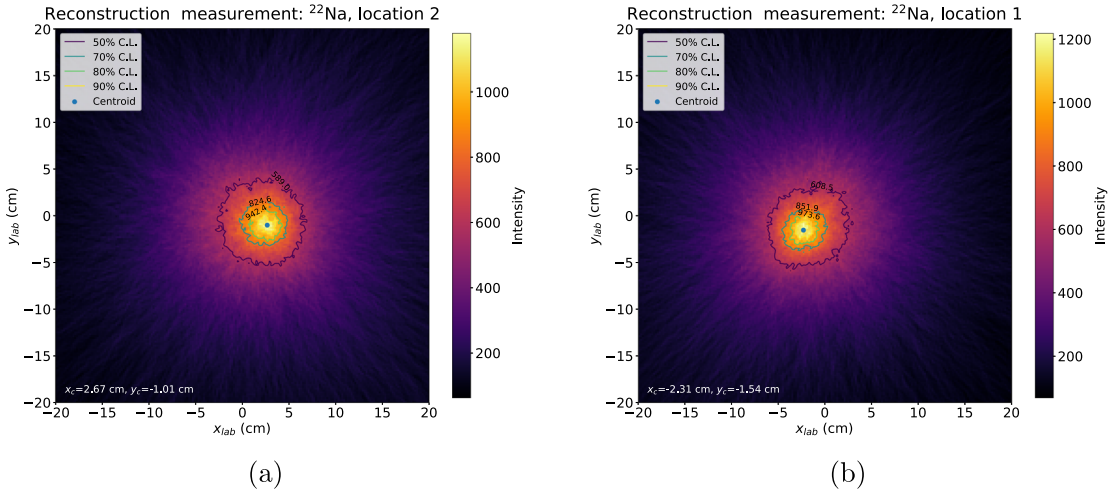

Figure 17. Compton-camera reconstruction onto a planar surface located at 10.5 cm from the sensor, using the 511 keV photon line of the ^{22}Na source; (a) and (b) show the reconstructed image at different lateral displacements. The contour levels at 50%, 70%, 80% and 90% of the maximum intensity are indicated together with the reconstructed source location. The observed shift of ∼5 cm is consistent with the manually adjusted displacement. The reconstructions were done from 4000 coincidences. No image correction was applied.

At 511 keV, we find an overall detection efficiency $\varepsilon_{511\ \mathrm{keV}} = (24.4 \pm 1.2)\,\%$, and a photopeak efficiency of $\varepsilon_{\mathrm{photo,\ 511\ keV}} = (7.0 \pm 0.5)\,\%$. Thus, photoabsorption contributes 29% to the overall detection efficiency, which is mainly determined by the Compton effect and the photoeffect. The measured efficiency is in excellent agreement with the estimate in [26]. The overall detection efficiency is 2.7 times larger than the value reported for a 2mm thick sensor attached to Timepix3 evaluated for a PET imaging prototype in [27]. Since therein coincident detection of both emitted 511 keV photons is required to create the line of response along which the annihilation took place, the measurement time (and radiation dose) with a 5 mm thick sensor t(5 mm) is reduced by $\frac{t(5\ \mathrm{mm})}{t(2\ \mathrm{mm})} = \frac{\varepsilon^2(2\ \mathrm{mm})}{\varepsilon^2(5\ \mathrm{mm})} = 0.13$ (by a factor of 7.3) to get the same amount of usable photon pairs. Application of the presented 3D reconstruction capability to reduce parallax errors could be the topic of future work.

In the same way, we estimate $\varepsilon_{1275\ \mathrm{keV}} = (6.8 \pm 0.4)\,\%$ and $\varepsilon_{\mathrm{photo,\ 1275\ keV}} = (0.53 \pm 0.03)\,\%$. At this energy, the relative contribution of the photoeffect to the total efficiency was found to be 8%.

5.3. Usage as a single-layer Compton camera (CC) and scatter polarimeter

Individual-particle detection, 3D reconstruction and a decent spectroscopic performance provide the means of using the device as a single-layer CC and scatter polarimeter [28], e.g. localization of γ-sources during nuclear decommissioning activities [29], or for studying γ-ray sources in astroparticle physics. Figure 17 shows CC reconstructions of the ^{22}Na source using the 511 keV γ-line for source placement at a distance of ∼10 cm from the detector and different lateral shifts. Therefore, we required the coincident detection (time window 200 ns) of the Compton electron (energy E_e and location $\vec{r}_e$) and scattered photon ($E_\gamma{}'$, $\vec{r}_\gamma{}'$). For each Compton event passing the condition $E_{\mathrm{total}} = (E_e + E_\gamma{}') \in [440,\ 580]$ keV, a cone was drawn around the axis defined by $\vec{r}_\gamma{}' - \vec{r}_e$ with its tip at $\vec{r}_e$ and an opening angle given by

$$\cos\beta = 1 - m_e c^2 \times \left(\frac{1}{E_\gamma{}'} - \frac{1}{E_{\mathrm{total}}}\right), \tag{9}$$

with $m_e c^2 = 511$ keV [30]. The intersections of the cones are back projected onto the source plane. Figures 17(a) and (b) compare the resulting images. The manually adjusted lateral displacement of ∼ 5cm can clearly be recognized. Single-layer CCs are compact, lightweight, do not require additional coincidencing schemes or proper alignment. Moreover, using a single sensor as scatterer and absorber, and profiting from high spatial granularity of the device, it is possible to cover almost the entire range of the scattering angles. Compared with the Timepix3-based single-layer CCs utilizing 2 mm thick CdTe/CZT (see e.g. [31]), the sensor studied in the present work offers a larger sensitive volume, thus a higher probability for the scattered photon to be detected. This will in particular increase sensitivity to lower dose rates at higher incident γ energy (>300 keV), which is the energy range where Compton scattering becomes dominant in CZT. Future work will focus on analysis methodology improvements in order to mitigate the effects of the incomplete charge collection. Therefore, machine learning approaches, e.g. assigning weights to each cone depending on measurable features, and image

post processing are considered. The required ground truth information will be obtained from simulation relying on the detector characterization results of the present work.

In addition to CC source location reconstruction, the polarization of the incoming photon field can be determined by evaluating the azimuthal angle between $\vec{r}_e$ and $\vec{r}_\gamma{}'$ within the reference system defined by the sensor [28, 32]. As discussed in [32], finer detector segmentation directly impacts the sensitivity to polarization. With a pixel pitch of 110 μm and ~240 μm 3D-spatial resolution (see section 5.1), the investigated device provides favorable parameters compared with current-date CZT scatter polarimeters, e.g. the IMARAD-PolCA instrument with 5 mm thickness at 2.5 mm pixel pitch, or Caliste-PolCA with 1 or 2 mm thick sensors at 580 μm [32]. Thus, future work should focus on evaluating the polarimetric performance of the presented device in simulation and experiment.

6. Conclusion

In the present work, a unique assembly of a Timepix3 detector with a 5 mm thick CZT sensor was studied in photon fields and relativistic charged particle beams. The high spatial segmentation and time resolution of the readout ASIC provided means to perform a detailed characterization of charge transport properties in the material. The combination of measurements with 'shallowly' interacting photons and penetrating particles allowed to measure $\overline{\mu_e \tau_e} = 1.3 \times 10^{-3}\,\mathrm{cm}^2/\mathrm{V}$ and the electron mobility $\mu_e = (944.8 \pm 1.3)\,\mathrm{cm}^2/\mathrm{V/s}$. Then the lifetime of electrons $\tau_e = (1.38 \pm 0.31)\,\mu$s was calculated. The sensor resistivity was measured to be $(0.155 \pm 0.02)\,\mathrm{GOhm} \cdot \mathrm{cm}$. The charge collection efficiency was presented as a function of the depth of interaction at different applied bias voltages. A drop by 30%–40% towards the common electrode was found, which was proposed to be due to a combination of charge carrier trapping and increased charge losses below the energy threshold of the pixels due to the lateral expansion of the charge clouds during the long drift. The incomplete charge collection was found to be a limiting factor for the spectroscopy of photons below ~120 keV, where the photo-peak positions differed for the case that the sensor was irradiated from the front or from the pixel-side. However, relative energy resolution of ~4.5% was found for photon energies above ~120 keV.

Moreover, the nanosecond-scale precision time measurement of Timepix3 allows reconstruction of particle interaction depths using previously developed analysis methodology. It was shown with a penetrating pion track, that a spatial resolution of ~240 μm can be achieved within the 5 mm thick sensor, while the extrapolation uncertainty amounts to 100 μm when evaluated at a distance of 1 m. We have found γ-ray detection efficiencies of $\varepsilon_{511\ \mathrm{keV}} = 24.4 \pm 1.2$ % and $\varepsilon_{1275\ \mathrm{keV}} = 6.8 \pm 0.4$ %, with relative photopeak contribution of 29% and 8%, respectively. A possible use of the detector as a single-layer Compton camera and scatter polarimeter is outlined.

Acknowledgments

The authors would like to thank the SPS team for providing Medipix collaboration with the beamtime for measurements with pions of 120 GeV/c. The authors are also thankful to Petr Mánek for helping with creating the proper pixel mask for the investigated detector. The authors thank Joe Ashby (University of Glasgow) and Yesid Mora for their technical effort in assembling the detector module. P.S. and B.B. were supported by the Czech Science Foundation's Junior Star grant with registration No. GACR GM23-04869M.

Data availability statement

The data cannot be made publicly available upon publication because they are not available in a format that is sufficiently accessible or reusable by other researchers. The data that support the findings of this study are available upon reasonable request from the authors.

ORCID iDs

P Smolyanskiy https://orcid.org/0000-0002-1122-1218
B Bergmann https://orcid.org/0000-0002-8076-5614
P Burian https://orcid.org/0000-0001-6907-7901
J Jelínek https://orcid.org/0009-0002-3588-6078
D Maneuski https://orcid.org/0000-0002-0890-7868
S Pospíšil https://orcid.org/0000-0001-5424-9096

References

[1] Poikela T *et al* 2014 *J. Instrum.* **9** C05013
[2] Medipix Collaboration https://medipix.web.cern.ch/home accessed on 2023
[3] Ballabriga R, Campbell M and Llopart X 2018 *Nucl. Instrum. Methods Phys. Res., Sect. A* **878** 10–23
[4] Schioppa E J 2014 The color of x-rays: spectral x-ray computed tomography using energy sensitive pixel detectors *CERN-THESIS-2014-179* Amsterdam U.
[5] Bergmann B, Pichotka M, Pospisil S, Vycpalek J, Burian P, Broulim P and Jakubek J 2017 *Eur. Phys. J.* C **77** 421
[6] Bergmann B, Burian P, Manek P and Pospisil S 2019 *Eur. Phys. J.* C **79** 1–12
[7] Turecek D, Jakubek J, Trojanova E and Sefc L 2018 *J. Instrum.* **13** C11022
[8] Carrel F, Schoepff V, Adeline Q, Amoyal G, Imbault M, Abou Khalil R, Bouzac Q, Mekhalfa Z, Tondut L and Faussier G 2018 *International conference on dismantling challenges: industrial reality, prospects and feedback experience*
[9] Fey J, Procz S, Schütz M, Schoepff V, Carrel F, Useche J, Fauler A and Fiederle M 2021 *J. Instrum.* **16** T07010
[10] Amoyal G, Ménesguen Y, Schoepff V, Carrel F, Michel M, Angélique J C and de Lanaute N B 2020 *IEEE Trans. Nucl. Sci.* **68** 229–35
[11] Llopart X, Ballabriga R, Campbell M, Tlustos L and Wong W 2007 *Nucl. Instrum. Methods Phys. Res., Sect. A* **581** 485–94
[12] Fey J, Procz S, Schütz M K and Fiederle M 2020 *Nucl. Instrum. Methods Phys. Res., Sect. A* **977** 164308
[13] Scienti O, Bamber J and Darambara D 2020 *IEEE Access* **8** 196541196541–52
[14] Bell R, Entine G and Serreze H 1974 *Nucl. Instrum. Methods* **117** 267–71
[15] Thomas B, Veale M, Wilson M, Seller P, Schneider A and Iniewski K 2017 *J. Instrum.* **12** C12045
[16] Kromek CZT detectors 2023 https://kromek.com/czt/
[17] Burian P, Broulím P, Jára M, Georgiev V and Bergmann B 2017 *J. Instrum.* **12** C11001
[18] Jakubek J 2011 *Nucl. Instrum. Methods Phys. Res., Sect. A* **633** S262–6
[19] Greiffenberg D *et al* 2019 *J. Instrum.* **14** P05020
[20] Jakubek J 2009 *Nucl. Instrum. Methods Phys. Res., Sect. A* **607** 192–5
[21] Krejci F *et al* 2016 *J. Instrum.* **11** C12026
[22] Schioppa E, Idarraga J, van Beuzekom M, Visser J, Koffeman E, Heijne E, Engel K and Uher J 2015 *IEEE Trans. Nucl. Sci.* **62** 2349–59
[23] Bergmann B, Azzarello P, Broulím P, Burian P, Meduna L, Paniccia M, Perrina C, Pospisil S, Tlustos L and Wu X 2020 *J. Instrum.* **15** C03013
[24] Mánek P, Bergmann B L, Burian P, Meduna L, Pospíšil S and Suk M 2019 Randomized Computer Vision Approaches for Pattern Recognition in Timepix and Timepix3 Detectors 1911.02367
[25] Bé M M *et al* 2016 *Table of Radionuclides* vol 8 (Monographie BIPM-5)
[26] Del Sordo S, Abbene L, Caroli E, Mancini A M, Zappettini A and Ubertini P 2009 *Sensors* **9** 3491–526
[27] Turecek D, Jakubek J, Trojanova E, Sefc L and Kolarova V 2018 *Nucl. Instrum. Methods Phys. Res., Sect. A* **895** 84–9
[28] Michel T, Durst J and Jakubek J 2009 *Nucl. Instrum. Methods Phys. Res., Sect. A* **603** 384–92
[29] Amoyal G, Schoepff V, Carrel F, Michel M, Blanc de Lanaute N and Angélique J 2021 *Nucl. Instrum. Methods Phys. Res., Sect. A* **987** 164838
[30] Manek P 2018 A system for 3d localization of gamma sources using timepix3-based compton cameras *Master thesis* Faculty of Mathematics and Physics Charles University
[31] Turecek D, Jakubek J, Trojanova E and Sefc L 2020 *J. Instrum.* **15** C01014
[32] Caroli E, Moita M, Da Silva R M C, Del Sordo S, De Cesare G, Maia J M and Pàscoa M 2018 *Galaxies* **6** 69